5-3. Contract Beamlines

BL22XU
JAEA Actinide Science I

1. Introduction

BL22XU is designed to promote basic and applied research on (1) actinide chemistry, (2) energy and environmental materials, (3) Fukushima environmental recovery and decommissioning, and related research. It was constructed in the Storage Ring and the RI Laboratory of SPring-8 to investigate radioactive materials containing sealed transuranium elements and nuclear fuel materials.

BL22XU has two double-crystal monochromators; one is a single cam-type monochromator with the multi-crystal switching system [1]. This monochromator can utilize wide-energy-range X-rays from 4 to 72 keV by using Si(111) and Si(311) crystals. The other is a calculation- and combination-type monochromator. This monochromator can utilize high-flux X-rays from 35 to 70 keV by using Si(111) crystals.

BL22XU has mirrors for focusing and higher harmonics rejection. They focus X-rays of 1 mm height and 3 mm width to 0.2 mm and 0.4 mm, respectively, in the RI Laboratory at a distance of 120 m from the light source. The three mirrors switch to reject higher harmonics of more than 7, 16, and 30 keV. A beryllium diffraction lens system for energies higher than 30 keV and a Kirkpatrick–Baez (KB) micro-focusing system for energies less than 40 keV are also used.

2. Experimental hutch 1 (EH1)

2-1. Diamond anvil-cell diffractometer

The diamond anvil-cell diffractometer is designed for both single-crystal and powder X-ray diffraction experiments under high pressure and low temperature. Equipped large-area two-dimensional detectors enable us to measure X-ray scattering patterns even at a high-Q range with a short exposure time. By using these detectors and high-energy monochromatic X-rays up to 70 keV, this diffractometer is also used for X-ray total scattering measurements to obtain the pair-distribution function (PDF).

The structural information of functional materials in local to middle-range structures has been regarded as important for understanding their properties. PDF analysis is one of the powerful methods to obtain that structural information. Our rapid-acquisition PDF measurement system has the advantage of obtaining high-statistics X-ray total scattering patterns with a short exposure time and has been applied to a wide variety of functional materials, such as hydrogen-absorbing materials [2], negative thermal expansion materials [3], and cement materials [4]. The N_2 gas flow device equipped with the diffractometer enables us to measure the X-ray total scattering patterns at the temperature range of 100–400 K. Recently, our system has succeeded in obtaining the temperature variation of PDFs of the giant negative thermal expansion material Ca_2RuO_4 and found a large local distortion in monoclinic phase [3]. The obtained PDF results contributed to the elucidation of the giant negative thermal expansion of Ca_2RuO_4.

2-2. Large diffractometer

Currently, an apparatus for Bragg coherent X-ray diffraction imaging (Bragg-CDI) is under development [5]. Bragg-CDI is expected to be a powerful technique for investigating individual nanosized crystalline particles. Furthermore, it is expected to enable studies of particles located within devices, which are inaccessible by electron beam techniques. This technique was developed to study particles as small as ~40 nm [6], which is the most interesting particle size.

In 2021, we developed a MEMS heating system for Bragg-CDI measurements and succeeded in observing the cubic-to-tetragonal phase transition of a 500-nm-sized single particle of $BaTiO_3$ crystal (BTO5) [7]. In the cubic phase, the three-dimensional structure of BT05 was successfully reconstructed. A clear strain distribution caused by dislocation inside the $BaTiO_3$ crystal was clearly visualized in the reconstructed image. The relationship between domain formation and dislocation was pointed out.

3. Experimental hutch 3 (EH3)

3-1. Hard X-ray photoemission spectroscopy (HAXPES)

The in situ photoemission spectroscopy of reaction processes in gas-phase atmospheres and high-temperature heating conditions is a powerful tool for understanding reaction processes such as catalytic reactions, metal oxidation, and so forth.

In FY2021, we upgraded to an atmosphere-controlled hard X-ray photoelectron spectroscopy (HAXPES) system. The gas-introduction devices enable us to perform HAXPES measurement under gas pressures below 1×10^{-4} Pa and temperatures from RT to 400˚C. As an example, the high-temperature oxidation process of a stainless-steel sample is shown in Fig. 1. This measurement was performed at 300˚C in an oxygen atmosphere (1×10^{-4} Pa). With time, the signal intensity of Si 1*s* increases, while that of Fe 2*p* decreases. This spectral change indicates both the diffusion and oxidation of Si on the Fe surface in a high-temperature oxidizing atmosphere.

Using this technique, we have started a study to elucidate the transport behavior of fission products (FPs) during a severe accident at the Fukushima Daiichi Nuclear Power Plant (1F). In particular, the in situ observation of the adsorption behavior of Cs, the most important FPs, was carried out on the reactor structural material (stainless steel).

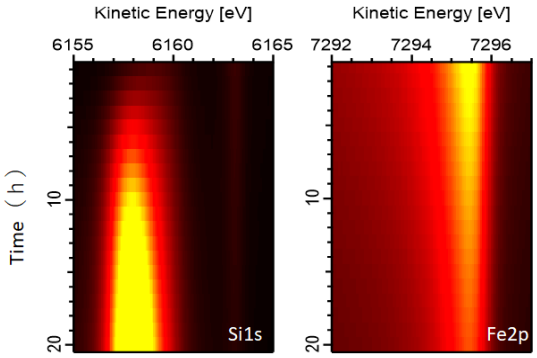

Fig. 1. HAXPES spectra of Si 1*s* (left) and Fe 2*p* (right) over time at high temperature (300˚C) and in oxidizing atmosphere (O_2: 1×10^{-4} Pa).

3-2. X-ray absorption fine structure (XAFS)

(1) XAFS analysis of high-temperature molten oxide

In the 1F accident, core fuel was heated beyond its melting point and reacted with the fuel cladding and core vessel. To analyze the progression of this severe accident, it is necessary to elucidate the properties of the fuel at high temperatures over the melting point. However, owing to the very high

melting point of UO_2 (3140 K), it is difficult to heat it up to the melting point. A method of heating a gas-suspended sample with a laser has been investigated, but this method requires a sample size of about 3 mm, making it difficult to transmit X-rays. Therefore, the XAFS measurement of the molten UO_2 has not been reported.

In this study, we investigated a method of heating a sample of about 0.5 mm thickness to a temperature above 3000 K by electrically heating it on a tungsten substrate. ZrO_2, whose melting point is 2988 K, was used as the sample. XAFS measurements were performed at the SPring-8 BL22XU beamline using the QXAFS system, which can acquire EXAFS regions of the Zr-K edge in 10 s. By using these systems, XAFS spectra of molten ZrO_2 were successfully obtained (Fig. 2). The spectral change corresponding to the change in the crystal system and the change into the molten state during the heating process were also observed. In the near future, we plan to measure the XAFS of the molten UO_2 as well. It will contribute to the decommissioning of the 1F and the analysis of the progression of the severe accident in the nuclear power plant.

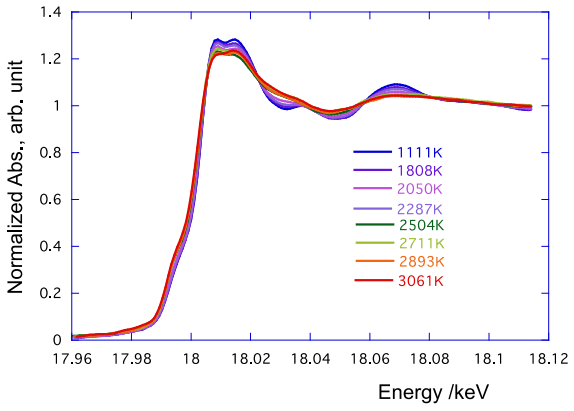

Fig. 2. XAFS spectra of heated ZrO_2.

(2) XAFS analysis for advanced vitrification technology

The high-level radioactive liquid waste (HLLW) generated in spent fuel reprocessing plants is mixed with a glass raw material (typically borosilicate glass) under a high-temperature molten state and disposed of as vitrified radioactive waste. The vitrification technology requires that more waste be maintained in a more stable state. Therefore, attempts have been made to optimize the composition of the raw glass. In the present work, we attempted to evaluate the effect of phosphorus addition, one of the composition improvement candidates, by the EXAFS analysis of cerium elements [8].

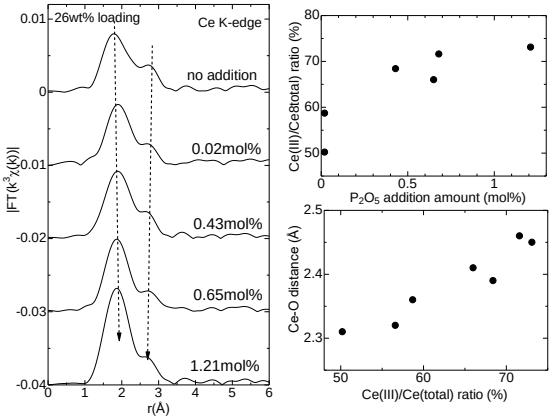

Fig. 3. Radial distribution function of Ce K-edge EXAFS of phosphorus-doped simulated glass (right), Ce-O distance (right-top), and ratio of trivalent cerium determined from L3 absorption edge XANES (right-bottom).

Figure 3 shows the results of EXAFS analysis of cerium elements in the simulated glass as a function of phosphorus addition. In the radial distribution function, a trend toward a gradual increase in the distance of the first peak and a shortening of the shouldered second peak was observed with phosphorus addition. It can be

interpreted as the reduction of cerium by phosphorus addition, weakening the attraction of the Ce–O correlation and the repulsion of the Ce–Si correlation. The results of this study show that the addition of a small amount of phosphorus has a strong reducing effect on glass. Since the solubility of cerium in borosilicate glass is much greater for the trivalent state than for the tetravalent state, the addition of phosphorus is favorable for the cerium elements in the simulated glass.

3-3. Stress/imaging measurements

In this device, deformation and state changes inside a material are determined by a diffraction method and an imaging method using high-energy synchrotron radiation X-rays. Figure 4 shows the diffraction pattern of pure copper (Cu) and S55C specimens with laser welding [9]. Diffraction patterns were roughly classified into five types and the focus is on (C) and (D). A diffraction pattern of the fcc structure was confirmed in the diffraction pattern of αFe (bcc structure) from S55C, but the lattice constant calculated from the diffraction pattern of fcc was smaller than that of copper. However, the austenitic phase (fcc structure) is not

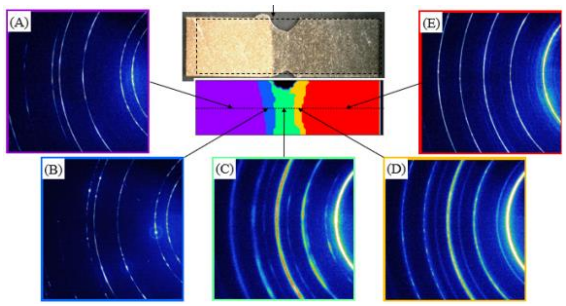

Fig. 4. Diffraction pattern of copper and S55C specimen with laser welding.

generated by the melting and solidification of S55C alone. Therefore, it is presumed that the fcc structure is retained austenite formed by dissolution with S55C after Cu penetrates into the S55C side by laser irradiation.

Recently, in order to observe the inside of fuel debris, we have been developing CT measurement technology using the absorption edge of X-rays. Figure 5 shows a three-dimensional image of zircon particles before and after immersion in each solution, as visualized by synchrotron X-ray microtomography with the energy around the Zr K-edge, i.e., 18.0 keV [10]. In this image, the lighter the region, the larger the line absorption coefficient, the higher the density, or the thicker the region. After immersing the samples in 0.1 M HCl (aq) and 0.1 M NaOH (aq), the enrichment of Zr on the surface was confirmed. When immersed in 0.1 M HCl (aq) and 0.1 M NaOH (aq), the surface of zircon dissolved in the solutions, and a substantial amount of dissolved Zr precipitated on the surfaces of the particles.

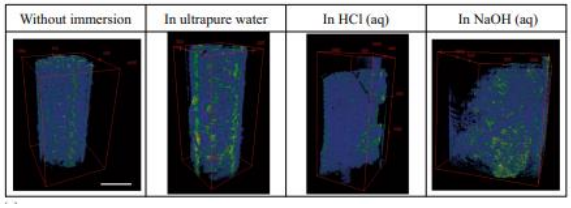

(a) 17.9 keV

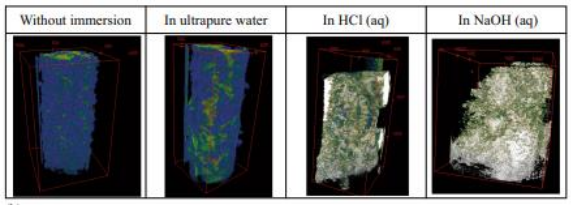

(b) 18.1 keV

Fig. 5. Three-dimensional image of zircon particles. The scale bar is 100 μm.

3-4. κ -type diffractometer

(1) Pair distribution function (PDF) analysis

It is generally difficult to obtain a solid solution that

combines substances with different structural stabilities in a single phase. A solid solution with ferroelectric barium titanate ($BaTiO_3$) and bismuth ferrite ($BiFeO_3$) as end members is one example, and it is difficult to prepare a single-phase sample. It is important to determine whether a sample is a single phase or not in order to improve the quality of ferroelectrics. Therefore, we have succeeded in developing a method of detecting trace amounts of segregated phases using a two-body correlation distribution function in addition to X-ray diffraction, which has been conventionally used to detect impurities [11]. In the X-ray diffraction pattern of the $BaTiO_3$-$BiFeO_3$ solid solution, it appears as a single phase with a rhombohedral structure. However, when the PDF was calculated from the obtained diffraction pattern, it was found that not only the component derived from the rhombohedral crystal structure calculated from the average structure but also the $BaTiO_3$ component was mixed and segregated (Fig. 6). By using PDF in this way, it has become possible to detect fine segregation phases on the nanoscale order.

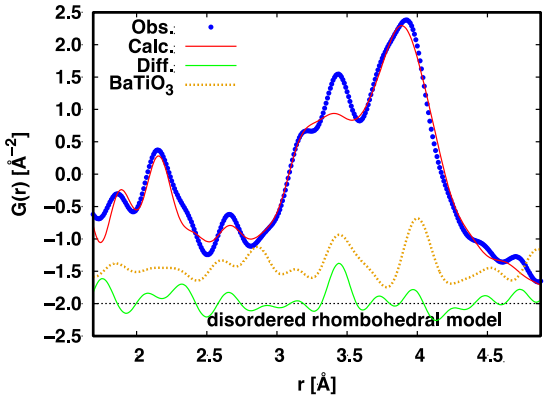

Fig. 6. Observed PDF for $BiFeO_3$—$BaTiO_3$ solid solution and pure $BaTiO_3$. The calculated PDF is assumed for a rhombohedral structure obtained by Rietveld refinement. Segregated $BaTiO_3$ is clearly observed.

(2) Surface structure diffractometer

Studies of various electrolyte/electrode interfaces were carried out using a κ-type multi-axis diffractometer. The interface structure of the all-solid-state Li-ion battery electrode during charge/discharge cycles, the interface structure of the electrocatalysis electrodes, and the electrode surface structure during the underpotential deposition reaction of Bi in an ionic liquid (IL) were studied. Here, we report the study of the electrodeposition reaction of Bi in 1-butyl-3-methylimidazolium tetrafluoroborate ([BMIM]BF4) on a Au(111) electrode using the surface X-ray scattering (SXS) technique. Previously, we continuously measured the width and position of the (10) peak during a potential scan. Both the position and width of the (10) peak did not change during the reaction, indicating that the deposited Bi atoms are not alloyed with surface Au atoms but may form superlattice structures on the Au electrode surface. In 2021, crystal truncation rod (CTR) measurements were carried out to elucidate the electrode/IL interface structure. First, the interface structure in the neat [BMIM]BF4 was investigated. The CTR profile measured at the potential, where the Bi UPD reaction occurs, was very different from that of the ideal surface, indicating that the Au(111) surface may be reconstructed or [BMIM]BF4 molecules may adsorb on the Au(111) surface. The fitting analysis revealed that the [BMIM]BF4 molecules (mainly BF4-) adsorb on the Au(111) electrode surface.

Tanida Hajime[*1], Machida Akihiko[*2], Ohwada Kenji[*2], Kobata Masaaki[*1], Kobayashi Tohru[*1], Okamoto Yoshihiro[*1], Shobu Takahisa[*1], Tominaga Aki [*1], Yoneda Yasuhiro [*1], and Tamura Kazuhisa[*1]

*1 Japan Atomic Energy Agency

*2 National Institutes for Quantum and Radiological Science and Technology

References:

[1] Shiwaku, H. et al. (2004). *AIP Conf. Proc.* **705**, 659.

[2] Ikeda, K. et al. (2021). *Appl. Sci*. **11**, 8349.

[3] Hu, L. et al. (2021). *Chem. Mater.* **33**, 7665.

[4] Im, S. et al. (2021). *J. Am. Ceram. Soc.* **104**, 4803.

[5] Ohwada, K. et al. (2019). *Jpn. J. Appl. Phys.* **58**, SLLA05.

[6] Oshime, N. et al. (2021). *Jpn. J. Appl. Phys.* **60**, SFFA07.

[7] Oshime, N. et al. (2022). *Jpn. J. Appl. Phys.* **61**, SN1008.

[8] Okamoto, Y. et al. (2022). *J. Nucl. Mater.* **570**, 153962.

[9] Shobu, T. Shiro, A. & Muramatsu T. (2021). *SPring-8 Document,* **D2021-013**, 318.

[10] Kitagaki, T. Yoshida, K. Liu, P. & Shobu, T. (2022). *npj Mater. Degrad.* **6**, 1.

[11] Yoneda, Y. et al. (2022). *Jpn. J. Appl. Phys*. **61,** SN1022.